Can segmented flow enhance heat transfer in microchannel heat sinks?

Amy Rachel Betz *, Daniel Attinger

Laboratory for Microscale Transport Phenomena, Department of Mechanical Engineering, Columbia University, New York, NY 10027, USA

ABSTRACT

Liquid cooling is an efficient way to remove heat fluxes with magnitudes up to 10,000 W/cm^2. One limitation of current single-phase microchannel heat sinks is the relatively low Nusselt number, due to laminar flow. In this work, we experimentally investigate how to enhance the Nusselt number with the introduction of segmented flow. The segmented flow pattern was created by the periodic injection of air bubbles through a T-junction into water-filled channels. We designed a polycarbonate heat sink consisting of an array of seven parallel microchannels each with a square cross-section 500 μm wide. We show that segmented flow increases the Nusselt number of laminar flow by more than 100%, provided the mass velocity of the liquid is within the range 330–2000 kg/m^2 s.

© 2010 Elsevier Ltd. All rights reserved.

1. Introduction

The concept of a microchannel heat sink was first introduced by Tuckerman and Pease [1] for the purpose of electronic cooling. As Fig. 1 shows, a microchannel heat sink is a device that removes heat, $\dot{Q}$, by fluid flowing in channels over a heated substrate (e.g. a computer chip). Tuckerman and Pease optimized the dimensions of the channels in terms of width and height for single-phase flow of water under the constraint of maximum allowable pressure drop and substrate surface temperature. They found that single-phase water-cooling could remove up to 790 W/cm^2. This heat flux required a mass velocity, G, of 5700 kg/m^2 s and a pressure drop of 220 kPa. A similar optimization process was done by Upadhye and Kandlikar [2], to minimize the pressure drop under the constraints of a given heat flux and maximum substrate temperature. They found that a water pressure drop below 10 kPa was sufficient to remove 100 W/cm^2 with an optimum channel geometry. One problem with single-phase flow heat transfer in microchannels is the low Nusselt number obtained in laminar flow [3], on the order of 4. Methods for increasing the Nusselt number include: surface area enhancement [4,5] by geometric obtrusions, tree-like bifurcating channels [6], large aspect ratio channels [1,7], serpentine channels to promote mixing and turbulence [8], short channels where the entrance region dominates [9,10], nano-fluids [11,12], and two-phase flow [4,7,13–17].

There is much interest in two-phase flow because the heat of vaporization is very high. It has been shown [18] that flow boiling can dissipate up to 10,000 W/cm^2 [13,16], which is 10 times more

heat than single-phase flow. While flow boiling is attractive because it delivers high heat flux at the constant temperature of the phase change, it can be difficult to control due to backflow and instabilities. Investigation into controlling the instabilities and backflow include the manufacturing of artificial nucleation sites [19], and inlet restrictions [16,20,21]. A drawback of boiling flow, where water is the working fluid, is that the saturation temperature is higher than the operating temperature of most electronics; the proposed solution is to use refrigerants as working fluids since the boiling temperature is lower than water. Refrigerants, however offer lower cooling capabilities due to a lower specific heat and heat of vaporization.

In this work, we investigate segmented flow as a way to enhance single-phase heat transfer with water in microchannels. Segmented flow is a periodic pattern of non-condensable bubbles and liquid slugs created at a T-junction by the injection of air in liquid-filled microchannels. The bubbles are typically longer than the channel diameter [22]. More details regarding the physics of the bubble breakup can be found in [22–25]. Segmented flow [22,26] has been widely used for chemical engineering applications where it increases mass transfer [27–30]. It should accordingly increase heat transfer, due to the same phenomenon of enhanced convection by recirculating wakes in the liquid slugs [29,31]. The presence of recirculating wakes requires surface tension to dominate over gravity, which occurs when the Bond number $\rho g d^2 / \sigma < 3.368$ [22]. In the work of Kreutzer et al. [29], a finite-element simulation was used to determine the liquid to solid mass transfer, for the case of catalyst removal from a monolith wall. From this work Kreutzer determined that the rate of mass transfer in the liquid slugs was 10 times the rate of laminar flow [29]. It has also been shown that the presence of bubbles increases the pressure

---

* Corresponding author. Tel.: +1 212 854 9125; fax: +1 212 854 3304.
E-mail address: arb2140@columbia.edu (A.R. Betz).

Nomenclature

A	area (m^2)	w	width (m)
B	hydraulic coefficient		
Ca	capillary number ($\mu U/\sigma$)	*Greek letters*	
c	specific heat (J/kg K)	α	fin enhancement factor
C	gas constant	α^*	aspect ratio
d	hydraulic diameter (m)	β	temperature difference (°C)
f	volumetric flow rate (m^3/s)	δ	film thickness (m)
f_r	friction factor	ε	liquid fraction
G	mass velocity (kg/m^2 s)	η	fin efficiency
h	convection coefficient (W/m^2 K)	θ	thermal resistance (K/W)
H	height (m)	μ	viscosity (Pa s)
k	thermal conductivity (W/m K)	ρ	density (kg/m^3)
K	minor loss term	σ	surface tension (N/m)
L	length (m)		
n	number of bubbles	*Subscripts*	
N	number of channels	B	bubble
p	pressure (Pa)	c	channel
P	perimeter (m)	G	gas
Pr	Prandtl number (ν/α)	L	liquid
Nu	Nusselt number (hd/k)	S	surface
Re	Reynolds number ($\rho U d/\mu$)	seg	segmented flow
$\dot{Q}$	heat flow (W)	sin	single-phase flow
q''	heat flux (W/m^2)	$slug$	liquid slug
T	temperature (°C)	sub	substrate
U	velocity (m/s)	w	wall
V	volume (m^3)		

drop in the channel due to the Laplace pressure at the liquid gas interface [27,29], a penalty that needs to be considered.

The presence of bubbles in the system presents an interesting engineering challenge. It may be desired, for industrial applications, to have a closed loop system, where water from the outlet is recirculated through a pump and a heat exchanger to the heat sink inlet; this process might necessitate to remove the air bubbles before the pump and re-inject air after the pump. Bubbles can indeed be removed from segmented flow by the addition of smaller capillary tubes downstream which remove the bubbles due to the difference in interfacial tension [32]. The use of a hydrophobic porous membrane parallel to the channel has also been shown by our group to effectively remove gas bubbles [33]. Further research regarding the removal of the bubbles would be useful for commercial implementation.
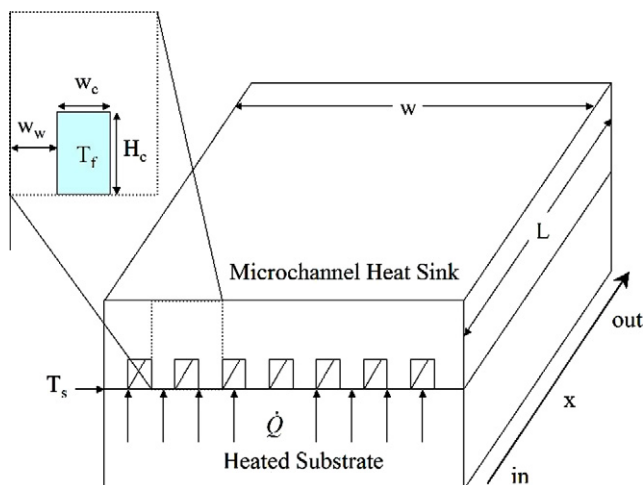
2. Theory

In this work, the 1D equivalent resistances method (Fig. 2) of Tuckerman and Pease [1] is used to calculate the performance of a micro heat sink (Fig. 1). In Fig. 2 the total thermal resistance θ_{total} is the ratio of $\Delta T = T_{S,max} - T_{L,in}$, the difference between the maximum heated substrate temperature and the fluid temperature at the inlet, over the power dissipated, $\dot{Q}$. The total thermal resistance, $\theta_{total} = \theta_{heat} + \theta_{conv}$, is the sum of a heat resistance and a convective resistance. The heat resistance in Eq. (1) is due to the heating of the fluid as it passes through the heat sink; it depends on volumetric flow rate f_L and specific heat capacity of the fluid (c_L).

$$\theta_{heat} = 1/(\rho_L c_L f_L). \tag{1}$$

Eq. (2) gives θ_{conv}, which is the resistance of the coolant fluid to heat convection. The expression for θ_{conv} is derived in [1] by treating the rectangular walls of a micro heat sink as fins with adiabatic bound-

Fig. 1. A microchannel heat sink in direct contact with a heated substrate (such as an integrated circuit chip).
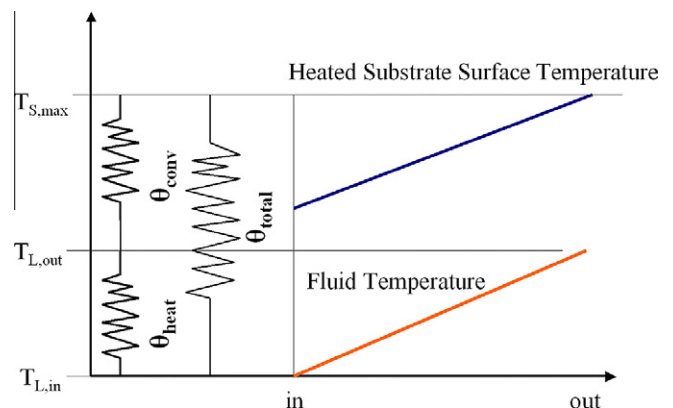

Fig. 2. Thermal resistances and temperature profile along the flow path for constant heat flux conditions.

ary conditions at their end, the fin efficiency η can be found by $\eta = \tan h(mH_c)/mH_c$, where $m = (Nuk_L/(k_fw_cw_w))^{1/2}$, as given by [1]. In Eq. (2), L_c is the channel length, w is the heat sink width, w_c is the channel width, w_w is the width between the channels, H_c is the channel height and $\alpha = 2H_c/(w_w + w_c)$ is the fin enhancement factor.

$$\theta_{conv} = (2/k_L Nu L_c w)(w_c/\alpha\eta). \tag{2}$$

From that modeling, the outlet temperature of the fluid and the maximum temperature of the substrate surface can be found based on the power dissipated $\dot{Q}$ and the inlet temperature of the fluid, as shown in Eqs. (3) and (4).

$$T_{L,out} = (\dot{Q}\theta_{heat}) + T_{L,in}, \tag{3}$$

$$T_{S,max} = (\dot{Q}\theta_{conv}) + T_{L,out}. \tag{4}$$

Several correlations are available for the Nusselt number and pressure drop, as presented below. They will be used to correlate our experiments for the respective single-phase and segmented flow case.

For single-phase, laminar, fully developed flow in rectangular channels with constant heat flux boundary conditions, Nu is calculated according to the correlation in Eq. (5) [3]:

$$Nu_{sin} = 8.235(1 - 2.0421(\alpha^*) + 3.0853(\alpha^*)^2 - 2.4765(\alpha^*)^3 + 1.0578(\alpha^*)^4 - 0.1861(\alpha^*)^5). \tag{5}$$

The aspect ratio is characterized by a parameter $\alpha^* = \min(H,w)/\max(H,w)$. In the case of square channels where $\alpha^* = 1$, this correlation yields Nu = 3.61. The Nusselt number of single-phase flow is expected to increase at higher Re due to the increasing thermal entry length. When the thermal entry length is no longer negligible, Nu can be found using a correlation by Lee and Garimella [10]. This correlation is valid for rectangular channels of any aspect ratio, constant heat flux boundary conditions, and laminar, hydrodynamically developed flow. When the hydrodynamic entry region is no longer negligible, correlations by Muzychka and Yovanovich [34] can be used to find Nu. Their work is valid for Pr > 0.1, uniform heat flux and constant surface temperature, and any channel cross-sections.

The pressure drop for single-phase flow is found using the Churchill correlation valid for both laminar and turbulent flow [35], given in Eq. (6), where d is the hydraulic diameter, K is the minor loss term and U_L is the liquid velocity.

$$\Delta p = \rho(4f_r L_c/d + K)U_L^2/2. \tag{6}$$

For segmented flow, Nu at constant heat flux was estimated with a correlation established from detailed multiphase flow simulations in cylindrical pipes by Lakehal et al. [28].

$$Nu_{seg} = Nu_{sin} + 0.022Pr^{0.4}Re_{seg}^{4/5}. \tag{7}$$

In Eq. (7), Nu_{sin} is the Nusselt number for single-phase fully developed liquid flow, found with Eq. (5), Pr is based on the properties of the liquid phase, and $Re_{seg} = d\rho_L U_B/\mu_L \cdot (L_B/(L_B + L_{slug}))$, where U_B is the bubble velocity and the definitions of L_B and L_{slug} are the respective length of the bubble and liquid slug, as shown in Fig. 3. Note that this definition is equivalent to the Reynolds number proposed in [28]. Eq. (7) is valid for well-defined gas bubbles when d is on the order of mm, Pr > 1, Re_{seg} is on the order of 1000, and 300 K < $(T_L)_{mean}$ < 340 K. Multiphase flow simulations in [28] revealed two mechanisms that increase Nu: the generation of the bubbles and the circulation in the liquid slugs. As mentioned in Section 1, a segmented flow with recirculating wakes can be generated provided the Bond number $\rho g d^2/\sigma < 3.368$ [22,29] and the capillary number Ca < 0.04 [29].

Other correlations for determining the Nusselt number of segmented flow were examined. As mentioned in Section 1, Kreutzer
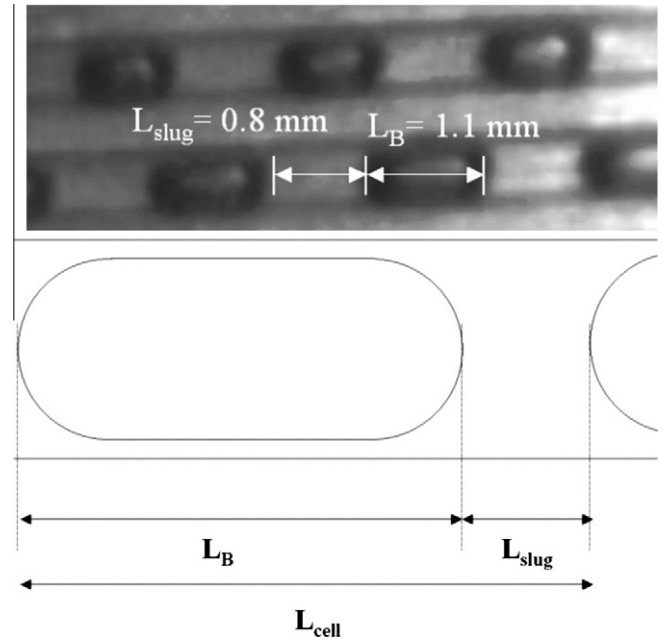

Fig. 3. Definition of L_B, L_{slug}, L_{cell}, with values for segmented flow at G_L = 670 kg/m² s.

et al. [29] obtained an expression for Nu from numerical simulation in square channels. Kreutzer's correlation is only valid when there is full circulation in the slugs and was only verified for Re < 300. Hetsroni et al. [36] conducted the first experimental work on the heat transfer of gas-liquid flow in microchannel heat sinks. They established correlations for the Nusselt number in triangular channels, valid for negligible entry length and Re < 100. In this work, we use the correlation of Lakehal et al. [28], which best reflects our experimental conditions in terms of Re and Ca range, flow patterns and entry length.

The pressure drop in segmented flow can be described with Eq. (8) [27], where a pressure drop term across the bubbles is added to the single-phase pressure drop for the liquid slugs. The pressure drop depends on two measurable quantities: the number of bubbles in a channel, n, and slug length, L_{slug} [27], as per Eq. (8).

$$\Delta p = n\left(\frac{U_B\mu}{d}\right)\left[\frac{B}{2}\left(\frac{L_{slug}}{d}\right) + C(3)^{2/3}(Ca)^{-1/3}\right]. \tag{8}$$

For square channels the hydraulic coefficient, B = 56.91, is used as well as C = 2.39, as determined by [37]. The capillary number, Ca, is determined by the bubble velocity [29,31,38].

$$Ca = U_B\mu_I/\sigma. \tag{9}$$

Parameters in Eqs. (7)–(9), such as L_{slug}, L_B and U_B, are available from high-speed visualizations in our experiments so that the experimental values of pressure drop and Nu can be compared with the correlations.

We also used Eqs. (7)–(9) to design the microchannel heat sink. In the design process, the bubble velocity is not known, and we propose the following process to determine U_B from an assumed water mass velocity G_L. We first assume a liquid volume fraction, ε = 0.5, and slug length L_s = 0.001 m, which are representative of our experiments as shown in Fig. 3. Assuming that the cross-section of the bubble is constant along its length, the bubble velocity is expressed by mass conservation [29–31].

$$U_B/U_{slug} = A_c/A_B. \tag{10}$$

With the slug velocity defined as $U_{slug} = G_L/\varepsilon\rho_L$ we obtain:
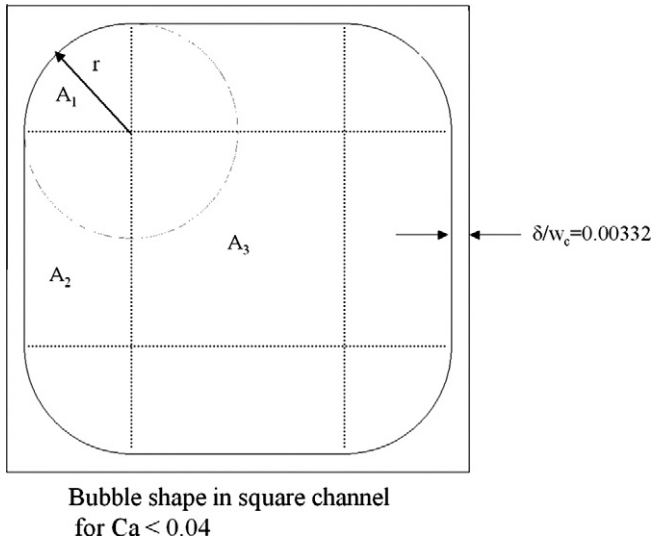
$$U_B = A_c G_L/(A_B\varepsilon\rho_L). \tag{11}$$

Fig. 4. Cross-sectional view of a bubble in a square channel at low Ca [29], with partitions for easier calculation of the area.

In Eq. (11) the only unknown parameter is the cross-sectional area of the bubble, A_B, which can be found as follows. Fig. 4 shows the typical cross-sectional shape of the bubble for Ca < 0.04 [29]. Assuming a cross-section shape as in Fig. 4, with a thin, constant film thickness δ along the walls and a thicker film at the edges with radius of curvature, $r = (w_c - 2\delta)/4$, the bubble area can be calculated by dividing the cross-section of the bubble into several contiguous subsections, as shown in Fig. 4, where $4A_1 = \pi(w_c - 2\delta)^2/16$, $4A_2 = (w_c - 2\delta)^2/2$ and $A_3 = (w_c - 2\delta)^2/4$ and the total bubble area is $A_B = 4A_1 + 4A_2 + A_3$. The film thickness δ is a function of the capillary number, Eq. (9), and is expressed by Eqs. (12) and (13) using a correlation based on the simulations of Hazel and Heil [38].

$$\delta = 0.00332 w_c \quad \text{for } 0.001 < \text{Ca} < 0.04, \tag{12}$$

$$\delta = -.0423 e^{(-\text{Ca}/5.3092)} - 0.1018 e^{(-\text{Ca}/0.3343)} + 0.1761 \quad \text{for Ca} > 0.04. \tag{13}$$

3. Design

A microchannel heat sink was designed in our laboratory to best demonstrate how segmented flow can enhance Nu in comparison with single-phase flow. Considering Fig. 2, the heat transfer enhancement is most noticeable under two conditions: first, θ_{conv} dominates over θ_{heat}, and second, the flow regime is such that there is a large difference between θ_{conv} for segmented and θ_{conv} for single-phase flow. For design purposes, we have plotted Eqs. (1) and (2) in Figs. 5–7 to show how the thermal resistances vary with liquid flow rate for typical channel diameters, with the same base area, $L = 0.025$ m and $w = 0.0075$ m and $w_w = w_c$. The Ca transition represents the point where Ca = 0.04, when the bubble cross-section changes from the non-axisymmetric shape shown in Fig. 4 to a more circular cross-section, which results in a dramatic decrease of circulation in the slug [28,29,39]. The Re transition represents the change from laminar to turbulent flow for the liquid flow rate. For 500 μm wide channels, Fig. 5 shows that the Reynolds number of the liquid flow must be greater than 60 in order to be in a regime where θ_{conv} dominates over θ_{heat}. Figs. 6 and 7 show the thermal resistances plotted for different channel widths, with the length remaining unchanged. For smaller geometries, such as 50 μm, shown in Fig. 6, θ_{heat} is the dominant resistance so that changes in Nu would not significantly modify the surface temperature, which is used to experimentally determine the Nusselt number. For larger widths, such as 2 mm, shown in Fig. 7, values of θ_{conv}
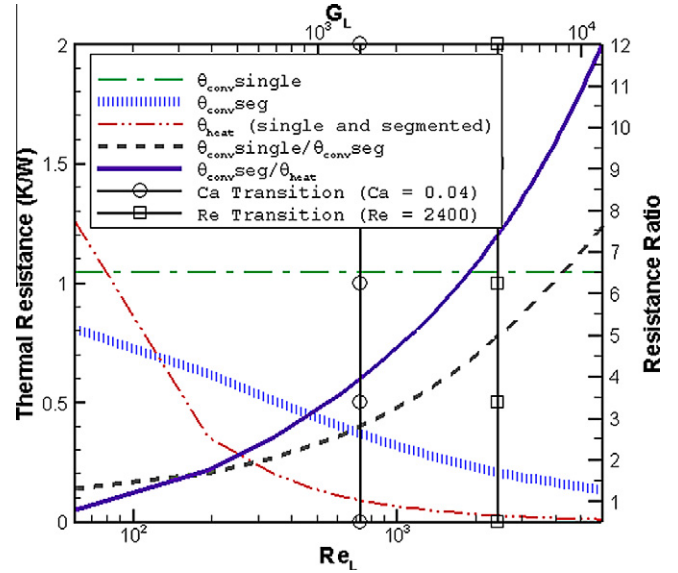

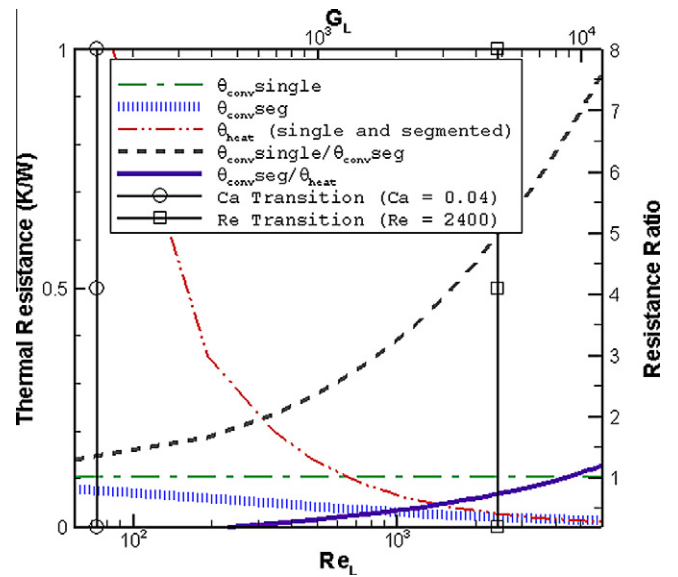**Fig. 5.** Thermal resistance plotted for a microchannel heat sink with seven parallel 500 μm channels, 25 mm in length.

Fig. 6. Thermal resistances plotted for a microchannel heat sink with 70 parallel 50 μm channels, 25 mm in length.

are much higher than in the 500 μm microchannel case, resulting in a less efficient heat sink.

4. Experimental setup

The microchannel heat sink and heated substrate are shown in Fig. 8. The heated substrate, made from aluminum, was designed to provide uniform heat flow. Before the single-phase and segmented flow measurements, a simple experiment was performed to quantify the heat loss of the heated aluminum block through the insulation, and verify that the surface temperature of the substrate can be found using a linear interpolation of the thermocouple measurements. The polycarbonate microchannnel heat sink was removed, so that the top surface of the aluminum block is exposed to air. The rest of the substrate is insulated with melamine foam approximately 2 cm thick, as shown in Fig. 9. An infrared
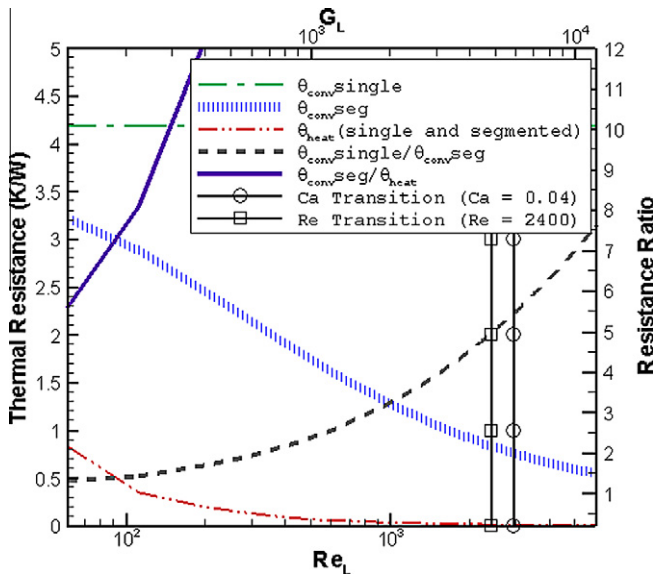
Fig. 7. Thermal resistances plotted for a mini channel heat sink with three parallel 2 mm channels, 25 mm in length.

pyrometer was used to measure the substrate temperature. Since the emissivity of aluminum is very low, 0.05, the surface of aluminum was painted black so that the emissivity was in the range of the pyrometer (a value of 0.95 was chosen). The natural convection heat transfer h was obtained by a correlation specific to small geometries and dependent on surface temperature, ranging from 15 to 25 W/m^2 K [40]. Five rows of three K-type thermocouples, as shown in Fig. 8b, were used to determine the surface temperature and temperature gradient using linear extrapolation. The test was run at five substrate temperatures: 50, 75, 90, 115, 150 °C. The maximum heat loss through the insulation $\dot{Q}_{loss}$ (see equation in Fig. 9) was found to be less than 1 W, which is negligible compared to the 40 W heat flux we apply during measurements involving fluid flow. The surface temperature was measured with a pyrometer and was found to correspond within 0.5 °C to the surface temperatures extrapolated from the set of five thermocouple measurements perpendicular to the surface. The standard deviation of the extrapolated values along the surface was less than 0.5 °C.

The microchannel heat sink (Fig. 8a) was milled from a polycarbonate slab, with a glass transition temperature of 150 °C, into seven parallel square channels with respective length and width of 25 mm and 500 μm. Polycarbonate was used since it is transparent and easy to manufacture. The heat sink was pressed on top of the heated substrate and sealed with an O-ring. It was heated with a constant power of 40 W and the water flow rate was varied from 238 to 3095 kg/m^2 s. Fig. 10 shows the experimental set up for the single-phase and segmented flow experiments.

The heated substrate and microchannel heat sink were insulated with melamine foam, as shown in Fig. 8c, with a typical loss
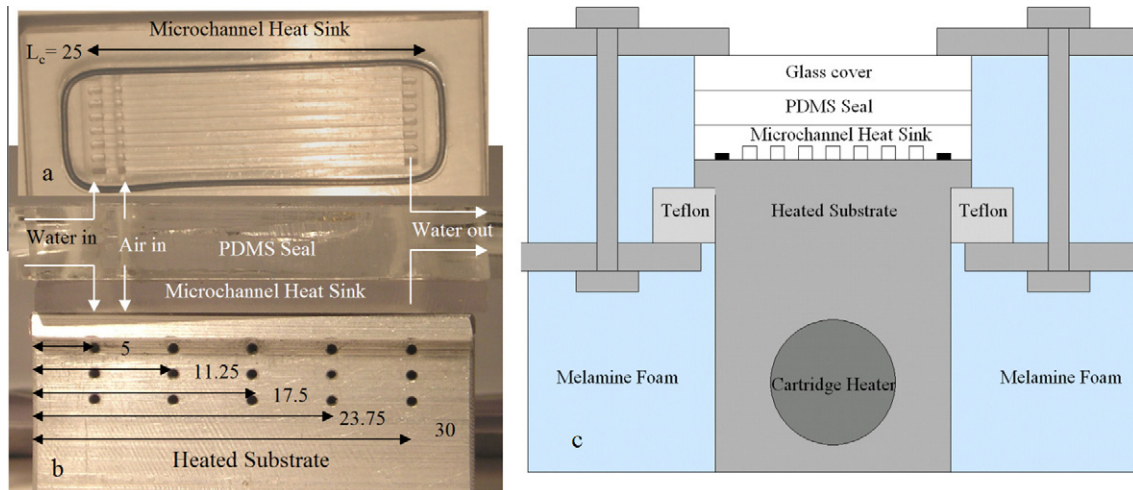

Fig. 8. (a) Microchannel heat sink with o-ring; (b) test setup with heated substrate showing thermocouple locations, with microchannel heat sink on top (all units are mm); and (c) cross-sectional view of test section.
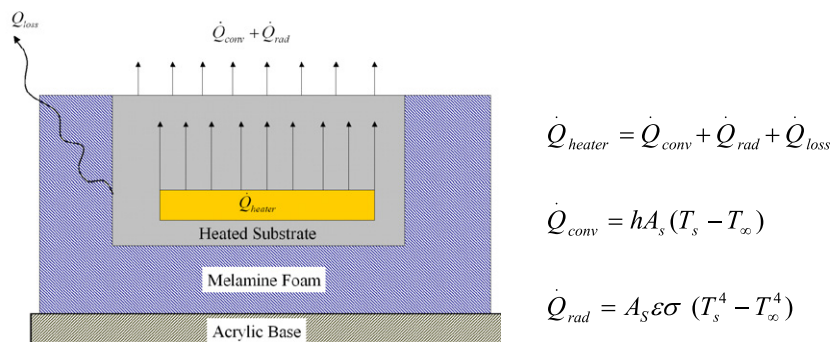

$$\dot{Q}_{heater} = \dot{Q}_{conv} + \dot{Q}_{rad} + \dot{Q}_{loss}$$

$$\dot{Q}_{conv} = hA_s(T_s - T_\infty)$$

$$\dot{Q}_{rad} = A_S \varepsilon \sigma \ (T_s^4 - T_\infty^4)$$

Fig. 9. Set up for energy balance verification, with corresponding equations.
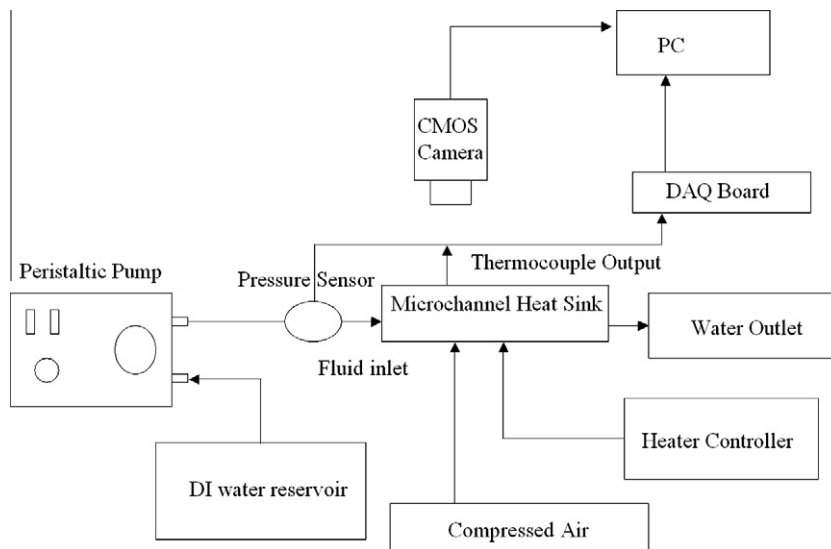
Fig. 10. Graphical representation of experimental setup.

measured as less than 1 W. The water was pumped with a peristaltic pump, and the liquid mass velocity G_L was found by measuring the fluid volume at the outlet over time. Bubbles were generated by injecting air through a slit at constant pressure using a Druck DPI 530 pressure regulator. The pressure was varied depending on G_L to produce a liquid fraction close to 0.5. The pressure drop along the channel was measured with a pressure transducer (Honeywell, 15 psi/105.53 kPa, ±0.087 psi/0.61 kPa uncertainty, 100 µs response time). Thermocouples (Type K, 0.5 mm diameter, Omega, 100 ms response time, ±0.5 °C uncertainty) recorded inlet and outlet temperatures of the fluid, along with 15 measurements on the substrate, as shown in Fig. 8b.

Table 1
Measured uncertainties.

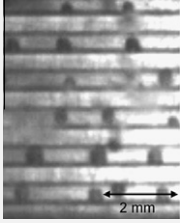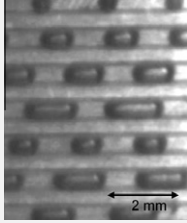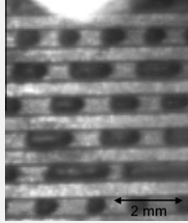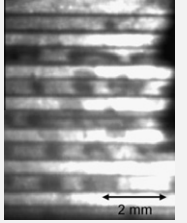| Variable	Maximum uncertainty absolute	Maximum relative uncertainty	Source
Pressure	±0.61 kPa	±32%, (5% typical, see Fig. 12)	Manufacturers Specs (Honeywell)
Temperature	±0.5 °C	±2.2%	Manufacturers Specs (Omega)
Heat flow	1 W	2.5%	Heat lost through insulation
Volumetric flow rate	0.2 mL/min	0.8%	Resolution limit
Channel dimensions	±5 µm	±1%	Resolution limit
Nusselt number	±0.504	±4%	Uncertainty propagation [42] on Eq. (14)
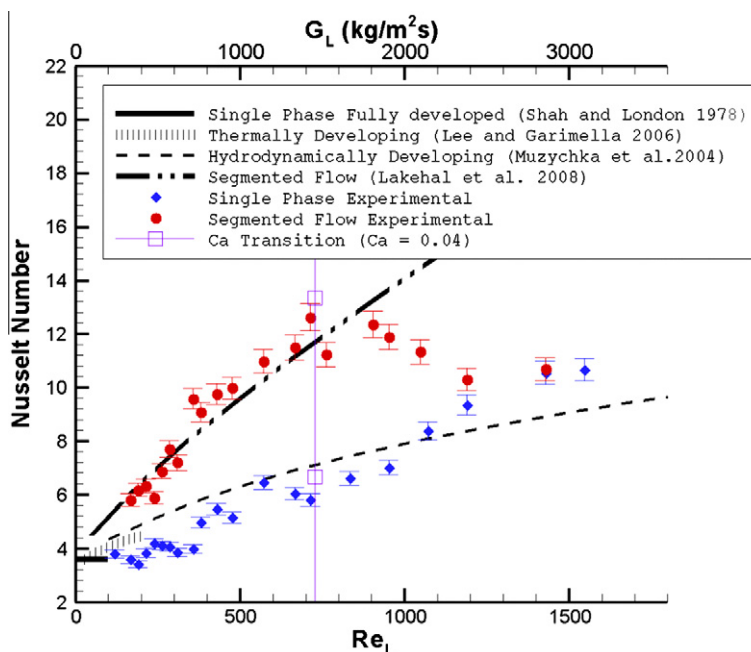
Fig. 11. Theoretical and measured values of Nusselt number for single-phase and segmented flow versus the Reynolds number based on the mass velocity of water.

Table 2
Visualization of four cases spanning three flow regimes with corresponding liquid mass velocity G_L. The liquid fraction, ε, can only be calculated precisely for slug flow using the method described in Section 2. In case d the low picture quality is due to the faster flow and limited frame rate of our camera.

Case	a	b	c	d
G_L (kg/m²s)	238.08	380.95	1333.33	3095
Flow regime	Bubbly	Slug	Slug	Churn
Average L_B (mm)	0.34	1.16	1.04	1.08
Average L_{slug} (mm)	No slug	0.93	0.79	No slug
ε	~0.8–0.9	0.482	0.47	~0.4–0.6
Increase in Δp (kPa)	Not measured	2.26	9.81	Not measured
Visualization				

5. Results and discussion

The convective heat transfer measurements were made using the heat sink described in the previous section at constant heating power of 40 W, and with water flow rates between 35 and 300 mL/min, corresponding to water mass velocities G_L of 300–3000 kg/m² s and Re_L from 160 to 1580, where Re_L is defined as $G_L d/\mu_L$ for both single-phase and segmented flow. Neglecting the low thermal losses through the insulation, as discussed in Section 4, the enthalpy change of the fluid can be replaced by the power supplied by the heater. An energy balance surrounding the channel provides the convection coefficient, h:

$$\dot{Q}_{heater} = (2\eta H_c + w_c)Nh \int_0^L \beta dx,\qquad(14)$$

where β, η and N are the temperature difference between the substrate and the fluid, the fin efficiency and the number of channels, respectively [7]. Since the first and last row of the thermocouples on the heated substrate correspond to the fluid inlet and outlet, the integral is discretized along the fluid flow direction into four sections using the trapezoidal rule.
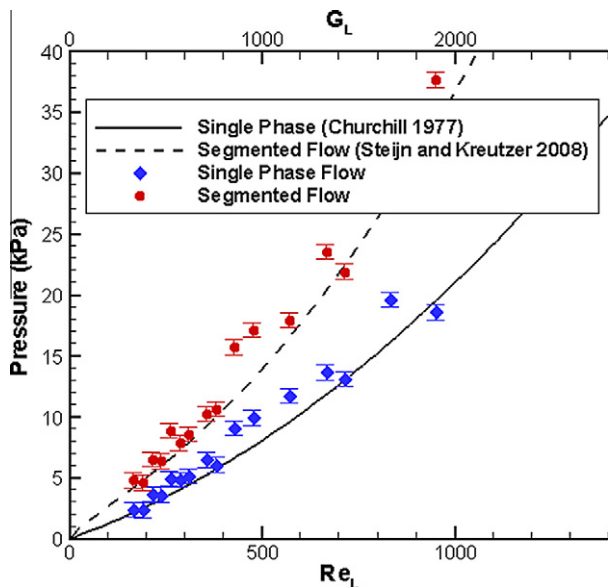

Fig. 13. Nusselt number expressed as a function of the pressure drop for single-phase and segmented flow.

Fig. 12. Theoretical and measured values of pressure drop for single-phase and segmented flow versus the Reynolds number based on the mass velocity of water.
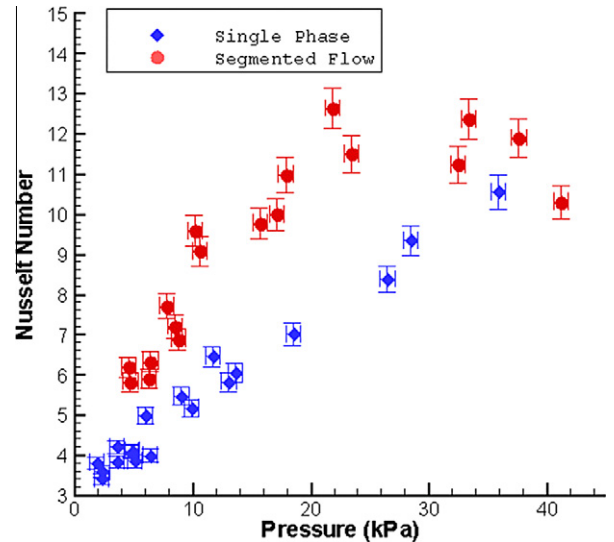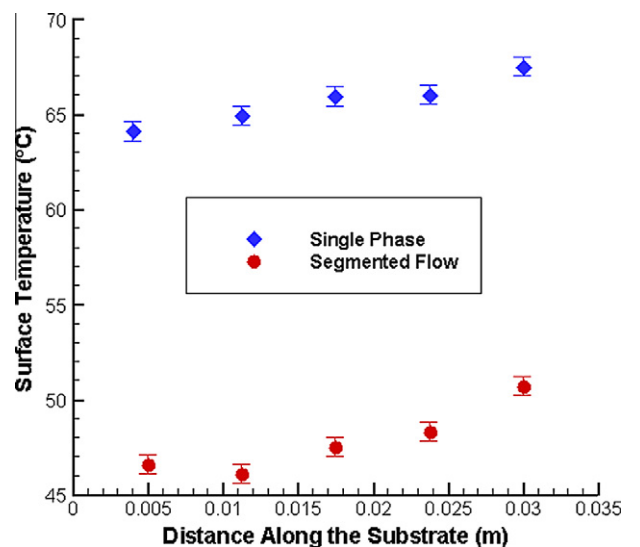

Fig. 14. Surface temperatures, T_s, along the flow direction, for a water flow rate of 75 mL/min, in the single-phase and segmented flow cases.

Table 3
Comparison of three modes of convective heat transfer.

Regime	G (kg/m^2 s)	q'' (W/cm^2)	Pressure drop (kPa)	Nusselt
Single-phase (this work)	238–3095	21	1.9–28.5	3.4–10.7
Segmented flow (this work)	333–2857	21	4.58–41.2	5.8–12.6
Boiling flow [7,17]	135–402	25–130	0.5–20	10.1–22.9

$$\int_0^L \beta dx = \sum_1^4 \left[\Delta x \left(\frac{\beta_i}{2} + \frac{\beta_{i+1}}{2} \right) \right] \quad \text{where } \Delta x = 0.00625 \text{ m.} \qquad (15)$$

A linear interpolation of the fluid is used to find the fluid temperature at the three interior points between the inlet and outlet temperatures, justified by the constant heat flux boundary conditions. Eq. (14) can be rearranged to solve for h as a function of the five surface temperatures and the inlet and outlet temperature of the fluid.

The Nusselt number is found from the heat transfer coefficient by Nu = hd/k_L, where k_L = 0.64 W/K m is the fluid thermal conductivity. The maximum uncertainty of the Nusselt number is ±4% due to the propagation of uncertainties in the temperature, geometry and thermal losses through the insulation. A summary of all uncertainties and their sources can be found in Table 1. Major contributors to the uncertainty are the thermocouple measurements and the heat flow measurement. For example, at G_L = 1140 kg/m^2 s, the average temperature difference β is 20 °C with an uncertainty of ±0.5 °C, or ±2.5%. Also, Section 4 shows that the uncertainty of $\dot{Q}_{heater}$ due to heat losses is less than 1 W, i.e. 2.5%. Fig. 11 shows that segmented flow increases the dimensionless heat transfer coefficient Nu up to 140% over single-phase flow, for values of G_L < 2000 kg/m^2 s, in very good agreement with the numerically obtained correlation of [28]. For flow rates higher than 2000 kg/m^2 s (or Re$_L \sim$ 1000), the heat transfer enhancement due to the segmented air bubble flow decreases quickly, and at G_L > 2500 kg/m^2 s (Re = 1200), the bubbles have no more influence on the heat transfer process. Interestingly, this transition starts at flow rates where the capillary number reaches the transition value of 0.04 (shown by a vertical bar), and the flow visualizations in Table 2 confirm a transition to churn flow. This might indicate that segmented flow enhances heat transfer provided the film between bubbles and wall does not become too thick, which would weaken the recirculation wakes, as explained in Section 3 and in [24,29–31]. As a side note, we were only able to produce segmented flow for values of G_L between 330 and 2850 kg/m^2 s. At lower G_L values segmented flow is replaced by bubbly flow (i.e. bubbles with diameters smaller than the channel diameter), and at higher G_L values a churn flow appears (fast bubbles with thick films, Ca reaching 0.04 and above, no heat transfer enhancement), in agreement with the data compiled by [22,41]. Visualization of these flow regimes can be seen in Table 2. The increasing values of the Nusselt numbers for single-phase flow at larger flow rates are very likely due to the non-negligible thermal and hydrodynamic entry lengths. As mentioned in Section 2 the correlations of Lee and Garimella [10] can be used to calculate Nu for thermally developing flow. In our experiments the thermal entry region accounts for 10% of the channel length at Re = 30. This correlation is only valid until Re $\sim$ 100, when the hydrodynamic entry becomes non-negligible. For cases where both thermal and hydrodynamic entry length are significant, the correlation of Muzychka and Yovanovich [34] should be used. Predictions from this correlation agreed very well with our experimental values for Re > 100 [34].

The penalty in pressure drop associated with segmented flow is evaluated in Fig. 12, which shows that segmented flow exhibits pressure drops higher than single-phase flow at the same prescribed liquid mass velocity, as predicted by the correlations in [27]. The segmented flow heat transfer enhancement scheme that we present here would only be of interest if it provides a higher Nusselt number than single-phase flow, for the same pressure drop. This is verified in Fig. 13, for pressure drop values ranging from 5 to 30 kPa, where the Nusselt number enhancement is about 50% using segmented flow rather than single-phase flow, for the same amount of pressure drop. This heat transfer enhancement is also seen with the lower measured substrate temperature shown in Fig. 14. Incidentally, Fig. 14 confirms that the temperature variation along the substrate increases linearly: this was expected since the fluid experiences a constant heat flux.

In Table 3, the pressure drop and Nusselt number of our segmented flow experiments are compared to single-phase and evaporative flow measurements with similar flow rate and heat flux. The flow boiling results are from the work of Qu and Mudawar [7,17], produced by an aluminum microchannel heat sink with 21 channels and a hydraulic diameter of 348.8 μm. Table 3 shows that segmented flow provides Nusselt number values in a range that is between single-phase and evaporative cooling.

6. Conclusion

Experiments and optimization studies have demonstrated that segmented flow could enhance heat transfer by up to 140% in a microchannel heat sink, in comparison with single-phase flow at the same liquid flow rate. The Nusselt number was used to characterize the improvement in heat transfer. Also, the pressure drop penalty in implementing segmented flow was reasonable, in the sense that, for the same values of pressure drop, segmented flow delivers a higher Nusselt number than single-phase flow. We determined that segmented flow would provide an intermediate step between single-phase and boiling flow for the purpose of electronic cooling. Also, we measured that the heat transfer enhancement only occurs for a specific range of flow rates and capillary numbers. At lower or higher capillary numbers, we explain that no significant heat transfer enhancement is observed because segmented flow is replaced by bubbly or churn flow, respectively.

References

[1] D.B. Tuckerman, R.F.W. Pease, High-performance heat sinking for VLSI, IEEE Electron Device Lett. EDL-2 (5) (1981) 126–129.

[2] H.R. Upadhye, S.G. Kandlikar, Optimization of microchannel geometry for direct chip cooling using single phase heat transfer, in: Proceedings of the Second International Conference on Microchannels and Minichannels (ICMM2004), 2004, pp. 679–685.

[3] R.K. Shah, A.L. London, Laminar Flow Forced Convection in Ducts: A Source Book for Compact Heat Exchanger Analytical Data, Academic Press, New York, 1978.

[4] S. Krishnamurthy, Y. Peles, Flow boiling water in a circular staggered micro-pin heat sink, Int. J. Heat Mass Transfer 51 (2008) 1349–1364.

[5] Y. Wang, Experimental investigation of heat transfer performance for a novel microchannel heat sink, J. Micromech. Microeng. 18 (2008).

[6] W. Escher, B. Michel, D. Poulikakos, Efficiency of optimized bifurcating tree-like and parallel microchannel networks in the cooling of electronics, Int. J. Heat Mass Transfer 52 (2008) 1421–1430.

[7] W. Qu, I. Mudawar, Flow boiling heat transfer in two-phase micro-channel heat sinks, Int. J. Heat Mass Transfer 46 (2003) 2755–2771.

[8] N. Rosaguti, Laminar flow and heat transfer in a periodic serpentine channel with semi-circular cross section, Int. J. Heat Mass Transfer 49 (2006) 2912–2923.

[9] Z. Tiantian, J. Li, Laminar flow characteristics in entry region in microchannels, in: 2008 Proceedings of the ASME Micro/Nanoscale Heat Transfer International Conference, MNHT 2008, 2008, pp. 1257–1264.

[10] P.-S. Lee, S.V. Garimella, Thermally developing flow and heat transfer in rectangular microchannels of different aspect ratios, Int. J. Heat Mass Transfer 49 (2006) 3060–3067.

[11] J. Lee, I. Mudawar, Assessment of the effectiveness of nanofluids for single-phase and two-phase heat transfer in micro-channels, Int. J. Heat Mass Transfer 50 (3–4) (2007) 452–463.

[12] T.-H. Tsai, R. Chein, Performance analysis of nanofluid-cooled microchannel heat sinks, Int. J. Heat Fluid Flow 28 (2007) 1013–1026.

[13] I. Mudawar, Assessment of high-heat-flux thermal management schemes, IEEE Trans. Compon. Pack. Schemes 24 (2) (2001).

[14] M.E. Steinke, S.G. Kandlikar, An experimental investigation of flow boiling characteristics of water in parallel microchannels, J. Heat Transfer (2004).

[15] B. Agostini, M. Fabbri, J. Park, L. Wojtan, J. Thome, State of the art of high heat flux cooling technologies, Heat Transfer Eng. 28 (4) (2007) 258–281.

[16] S. Kandlikar, High heat flux removal with microchannels – a roadmap of challenges and opportunities, Heat Transfer Eng. 26 (8) (2005) 5–14.

[17] W. Qu, I. Mudawar, Measurement and prediction of pressure drop in two-phase micro-channel heat sinks, Int. J. Heat Mass Transfer 46 (15) (2003).

[18] I. Mudawar, M.B. Bowers, Ultra-high critical heat flux (CHF) for subcooled water flow boiling-I: CHF data and parametric effects for small diameter tubes, Int. J. Heat Mass Transfer 42 (8) (1999) 1405–1428.

[19] C.-J. Kuo, A. Kosar, Y. Peles, S. Virost, C. Mishra, M. Jensen, Bubble dynamics during boiling in enhanced surface microchannels, J. Micromech. Microeng. 15 (6) (2006) 1514.

[20] C.-J. Kuo, Y. Peles, Pressure effects on flow boiling instabilities in parallel microchannels, Int. J. Heat Mass Transfer 52 (1–2) (2009) 271–280.

[21] A. Kosar, C.J. Kuo, Y. Peles, Suppression of boiling flow oscillations in parallel microchannels by inlet restrictors, J. Heat Transfer 128 (3) (2006) 251–260.

[22] C. Weinmueller, N. Hotz, A. Mueller, D. Poulikakos, On two-phase flow patterns and transition criteria in aqueous methanol and CO_2 mixtures in adiabatic, rectangular microchannels, Int. J. Multiphase Flow 35 (8) (2009) 760–772.

[23] T. Cubaud, C.-M. Ho, Transport of bubbles in square microchannels, Phys. Fluids 16 (12) (2004).

[24] A. Gunther, S.A. Khan, M. Thalmann, F. Trachsel, K.F. Jensen, Transport and reaction in microscale segmented gas liquid flow, Lab on a Chip 4 (2004) 278–286.

[25] M.D. Menech, P. Garstecki, F. Jousse, H.A. Stone, Transition from squeezing to dripping in a microfluidic T-shaped junction, J. Fluid Mech. 595 (2008) 141–161.

[26] T. Thorsen, R.W. Roberts, F.H. Arnold, S.R. Quake, Dynamic pattern formation in a vesicle-generating microfluidic device, Phys. Rev. Lett. 86 (18) (2001) 4163–4166.

[27] V. Steijn, M. Kreutzer, Velocity fluctuations of segmented flow in microchannels, Chem. Eng. J. 135S (2008) 159–165.

[28] D. Lakehal, G. Larrignon, C. Narayanan, Computational heat transfer and two-phase topology in miniature tubes, Microfluid Nanofluid 4 (2008) 261–271.

[29] M.T. Kreutzer, F. Kapteijn, J.A. Moulijn, J.J. Heiszwolf, Multiphase monolith reactors: chemical reaction engineering of segmented flow in microchannels, Chem. Eng. Sci. (60) (2005) 5895–5916.

[30] W.L. Chen, Gas–liquid two-phase flow in micro-channels, Int. J. Multiphase Flow 28 (2002) 1247–1253.

[31] T.C. Thulasidas, M.A. Abraham, R.L. Cerro, Bubble-train flow in capillaries of circular and square cross section, Chem. Eng. Sci. 50 (2) (1994) 183–199.

[32] A. Gunther, M. Jhunjhunwala, M. Thalmann, M.A. Schmidt, K.F. Jensen, Micromixing of miscible liquids in segmented gas–liquid flow, Langmuir 21 (4) (2005) 1547–1555.

[33] J. Xu, R. Vaillant, D. Attinger, Porous membrane for bubbles removal in microfluidic channels: physical mechanisms and design criteria, Microfluid Nanofluid (in review).

[34] Y.S. Muzychka, M.M. Yovanovich, Laminar forced convection heat transfer in the combined entry region of non-circular ducts, ASME J. Heat Transfer (2004).

[35] S.W. Churchill, Friction-factor equation spans all fluid-flow regimes, Chem. Eng. (New York) 84 (24) (1977) 91–92.

[36] G. Hetsroni, A. Mosyak, E. Pogrebnyak, Z. Segal, Heat transfer of gas–liquid mixture in micro-channel heat sink, Int. J. Heat Mass Transfer 52 (2009) 3963–3971.

[37] H. Wong, C.J. Radke, S. Morris, The motion of long bubbles in polygonal capillaries, part 2 Drag, fluid pressure and fluid flow, J. Fluid Mech. 292 (1995) 95–110.

[38] A.L. Hazel, M. Heil, The steady propagation of a semi-infinite bubble into a tube of elliptical or rectangular cross-section, J. Fluid Mech. 470 (2001) 91–114.

[39] V. Ajaev, G.M. Homsy, Modeling shapes and dynamics of confined bubbles, Ann. Rev. Fluid Mech. 38 (2006) 277–307.

[40] M. Miyamoto, Y. Katoh, J. Kurima, S. Kurihara, K. Yamashita, Free convection heat transfer from vertical and horizontal short plates, Int. J. Heat Mass Transfer 28 (9) (1985) 1733–1745.

[41] A. Gunther, K.F. Jensen, Multiphase microfluidics: from flow characteristics to chemical and material synthesis, Lab on a Chip 6 (2006) 1487–1503.

[42] R.S. Figiola, D.E. Beasley, Theory and Design for Mechanical Measurements, fourth ed., Wiley, Hoboken, 2006.